

LOW LUMINOSITY STATES OF THE BLACK HOLE CANDIDATE GX 339–4. II. TIMING ANALYSIS

MICHAEL A. NOWAK¹, JÖRN WILMS², JAMES B. DOVE^{1,3}

To Be Published in The Astrophysical Journal

ABSTRACT

Here we present timing analysis of a set of eight Rossi X-ray Timing Explorer (RXTE) observations of the black hole candidate GX 339–4 that were taken during its hard/low state. On long time scales, the RXTE All Sky Monitor data reveal evidence of a 240 day periodicity, comparable to timescales expected from warped, precessing accretion disks. On short timescales all observations save one show evidence of a persistent $f_{\text{QPO}} \approx 0.3$ Hz QPO. The broad band (10^{-3} – 10^2 Hz) power appears to be dominated by two independent processes that can be modeled as very broad Lorentzians with $Q \lesssim 1$. The coherence function between soft and hard photon variability shows that if these are truly independent processes, then they are individually coherent, but they are incoherent with one another. This is evidenced by the fact that the coherence function between the hard and soft variability is near unity between 5×10^{-3} – 10 Hz but shows evidence of a dip at $f \approx 1$ Hz. This is the region of overlap between the broad Lorentzian fits to the PSD. Similar to Cyg X–1, the coherence also drops dramatically at frequencies $\gtrsim 10$ Hz. Also similar to Cyg X–1, the hard photon variability is seen to lag the soft photon variability with the lag time increasing with decreasing Fourier frequency. The magnitude of this time lag appears to be positively correlated with the flux of GX 339–4. We discuss all of these observations in light of current theoretical models of both black hole spectra and temporal variability.

Subject headings: accretion — black hole physics — Stars: binaries — X-rays: Stars

1. INTRODUCTION

In a companion paper to this work (Wilms et al. 1998a; hereafter paper I) we have presented spectral analysis of a series of Advanced Satellite for Cosmology and Astrophysics (ASCA) and simultaneous radio/Rossi X-ray Timing Explorer (RXTE) observations of the black hole candidate (BHC) GX 339–4. This source has exhibited both spectrally soft states (cf. Grebenev et al. 1991; Miyamoto et al. 1991) and spectrally hard states (cf. Grebenev et al. 1991; Miyamoto et al. 1992; Zdziarski et al. 1998). Both the ASCA and RXTE observations presented in paper I showed GX 339–4 to be in spectrally hard and low luminosity (3 – 9 keV flux $\lesssim 10^{-9}$ ergs cm^{–2} s^{–1}) states. The eight RXTE observations spanned roughly a factor of five in terms of observed 3 – 9 keV flux.

In this work we shall consider the timing analysis of the eight RXTE observations. Timing analysis for GX 339–4 previously has been presented for the soft, bright ‘very high state’ (Miyamoto et al. 1991), the soft, fainter ‘high state’ (Grebenev et al. 1991), and the hard ‘low state’ (Grebenev et al. 1991; Miyamoto et al. 1992). In addition, timing analysis has been presented for so-called ‘intermediate states’, which are bright but spectrally harder than the typical ‘very high’ or ‘high states’ (Méndez & van der Klis 1997). In general, the harder states exhibit more temporal variability than the softer states (cf. van der Klis 1989). Timing analyses of the GX 339–4 hard state have shown similar results to analyses of other hard state BHC (Miyamoto et al. 1992). Specifically, the GX 339–4 temporal variability has been observed to be similar to that of Cygnus X–1 (Belloni & Hasinger 1990a; Belloni & Hasinger 1990b; Miyamoto et al. 1992; Nowak et al. 1998a, and references therein).

A discussion of Fourier techniques in specific, and timing

analysis in general, has been presented by van der Klis (1989). Here we apply these Fourier analysis techniques in the same manner as for our RXTE observations of Cyg X–1 (Nowak et al. 1998a). Specifically, we used the same techniques for estimating: deadtime corrections (Zhang et al. 1995; Zhang & Jahoda 1996); the error bars and Poisson noise levels of the Power Spectral Density (PSD) (Leahy et al. 1983; van der Klis 1989); the error bars and noise levels for the coherence function (Bendat & Piersol 1986; Vaughan & Nowak 1997); and the error bars and noise levels for the Fourier frequency-dependent time lag between hard and soft photon variability (Bendat & Piersol 1986; Nowak et al. 1998a). A self-contained discussion of these techniques as regards RXTE timing analysis is given by Nowak et al. (1998a).

This paper is organized as follows. First we consider evidence for long term periodicities in the RXTE All Sky Monitor (ASM) data in section 2. In section 3 we consider the Power Spectral Density (PSD). In section 4 we consider both the coherence function (cf. Vaughan & Nowak 1997) and the Fourier frequency-dependent time lags between hard and soft photon variability. We discuss the theoretical implications of these observations in section 5. We then summarize our results in section 6.

2. ALL SKY MONITOR OBSERVATIONS OF LONG ‘CHARACTERISTIC TIMESCALES’ IN GX 339–4

We used data from the All Sky Monitor on RXTE to study the long-term behavior of GX 339–4. The ASM is an array of three shadow cameras combined with position sensitive proportional counters that provides for a quasi-continuous coverage of the sky visible from RXTE. In practice, lightcurves in three energy bands — 1.3 – 3.0 keV, 3.0 – 5.0 keV, and 5.0 – 12.2 keV — as well as over the whole ASM band are publically available from

¹JILA, University of Colorado, Campus Box 440, Boulder, CO 80309-0440, USA; {mnowak, dove}@rocinate.colorado.edu

²Institut für Astronomie und Astrophysik, Abt. Astronomie, Waldhäuser Str. 64, D-72076 Tübingen, Germany; wilms@astro.uni-tuebingen.de

³also, CASA, University of Colorado, Campus Box 389, Boulder, CO 80309-0389, USA

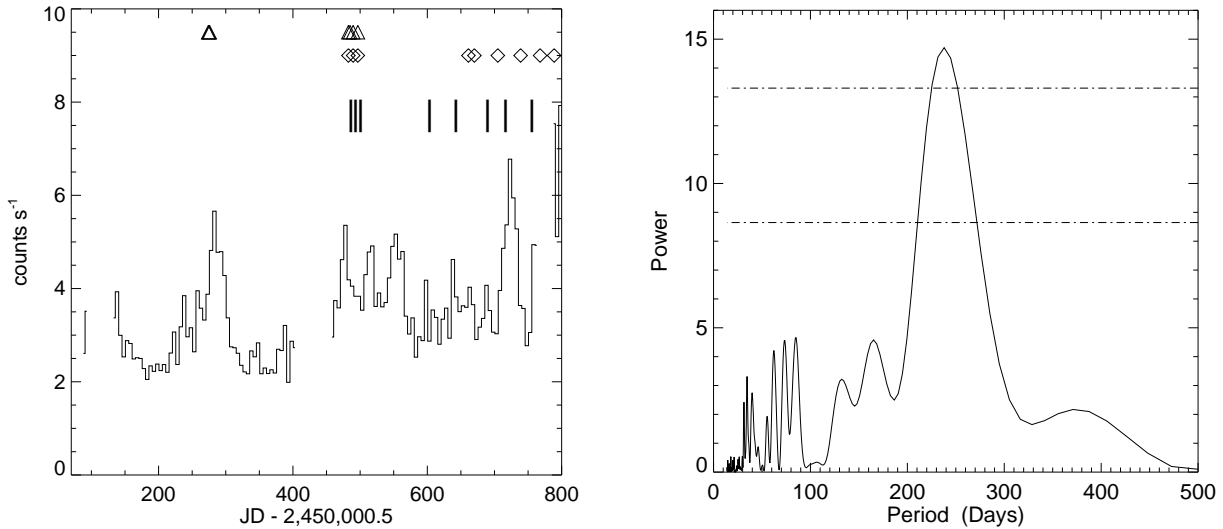


FIG. 1.— *Left*: RXTE All Sky Monitor data for GX 339–4 (5 day averages in the 1.3–12.2 keV band) vs. Truncated Julian Date (TJD) \equiv Julian Date (JD) – 2450000.5. Dashes indicate dates of our RXTE pointed observations, diamonds indicate dates of MOST observations (Hannikainen et al. 1998), and triangles indicate dates of ATCA radio observations (Corbel et al. 1998). *Right*: A Lomb-Scargle Periodogram (cf., Lomb 1976, Scargle 1982) of the ASM data for TJD < 800. We have used 600 periods ranging from 2 weeks to 500 days. Lines are estimates of the 99.9% and 90% significance levels.

the ASM data archives (Lochner & Remillard 1997). Typically there are several 90 s measurements available for each day. Further descriptions of the instrument and first year results are presented by Levine et al. (1996) and Remillard & Levine (1997).

In Figure 1 we present the ASM data of GX 339–4 up until Truncated Julian Date (TJD) \approx 800 (1997 November 15). See paper I for a presentation of the complete to date ASM data of GX 339–4. We also indicate in this figure the dates of our RXTE observations, as well as the dates of Australian Telescope Compact Array (ATCA) and Molongolo Observing Synthesis Telescope (MOST) radio observations of GX339–4 (Fender et al. 1997; Corbel et al. 1997; Hannikainen et al. 1998; paper I). The average 1σ error bar for a point presented in Figure 1 is ≈ 0.4 cts s^{-1} . Note the three peaks (at TJD \approx 280, 480–580, 780) in the ASM data that occur at intervals separated by ≈ 250 days.

We determined the significance of any possible long term periodicities in the ASM light curves by computing the Lomb-Scargle Periodogram (Lomb 1976; Scargle 1982) for the 1.3–12.2 keV band for 5-day average data. Here we only average data where the best fit to the source position and flux in an ASM observation has a $\chi^2_{\text{red}} \leq 1.5$ (cf. Lochner & Remillard 1997) in *each* of the three ASM energy channels. We only considered ASM data taken before TJD 800, as GX 339–4 underwent a state change shortly thereafter (see paper I). The periodogram shown in Figure 1 reveals evidence of a 240 day period at greater than the 99.9% significance level. [The significance levels were estimated following the methods of Horne & Baliunas (1986).] Epoch folding (cf. Leahy et al. 1983; Schwarzenberg-Czerny 1989; Davies 1990) of the ASM lightcurves also shows evidence of this 240 day periodicity.

Long timescale periodicities and quasi-periodicities are relatively common in ASM observations of binary sources (Remillard 1997, Private Communication). Evidence for a 294 d periodicity in Cygnus X–1 has been previously reported (Kemp et al. 1983; Priedhorsky, Terrell & Holt 1983), and is readily ap-

parent in the ASM data during the hard state. A 198 day periodicity also has been observed in LMC X–3 (Cowley et al. 1991; Wilms et al. 1998b). We note that the observed timescales of these periodicities are comparable to the timescales expected from the the radiation pressure driven warping instability discovered by Pringle (1996) (see also Maloney, Begelman & Pringle 1996; Maloney & Begelman 1997; Maloney, Begelman & Nowak 1998). This is a fairly generic instability that causes a radiatively efficient (i.e., non-advection dominated) accretion disk to warp and precess on $\mathcal{O}(100 \text{ day})$ timescales. Such a timescale is consistent with the periodicities seen in many binaries and with the 240 periodicity that we see in GX 339–4.

As discussed in paper I, however, both the Compton corona models and the ADAF models of the spectral data suggest that the observed flux variations are in large part attributable to variations of the coronal radius. A pure warped, precessing disk model would invoke only inclination angle effects. This is unlikely to be the case for GX 339–4. As discussed by Maloney, Begelman & Pringle (1996), however, the precession timescale and warp shape are more sensitive to the outer boundary conditions than the inner boundary conditions. Perhaps then it is possible that what we observe is a combination of a quasi-steadily precessing disk on large radii combined with coronal structure changes on small radii. Although 240 days is a characteristic timescale in both the Lomb-Scargle periodogram and in the epoch folding analysis, it is obvious from Figure 1 that we are not observing a strictly periodic phenomenon.

3. POWER SPECTRAL DENSITIES

We studied the variability of GX 339–4 using data from the Proportional Counter Array (PCA) on-board RXTE. The PCA consists of five nearly identical co-aligned Xenon proportional counter units (PCUs) with a total effective area of about 6500 cm^2 , and it is sensitive in the energy range from 2 keV to $\sim 60 \text{ keV}$ (Jahoda et al. 1996). We only used data where all five PCUs were turned on, and where the elevation angle between

the spacecraft pointing direction and the limb of the earth was greater than 10° . PCA count rates for the GX 339–4 observations ranged from 200 to 800 cts s^{-1} , and were of $\mathcal{O}(10\text{ks})$ duration.

To study the short timescale variability, we created 2^{-8} s resolution lightcurves in 4 different energy bands: 0–3.9 keV, 3.9–7.5 keV, 7.5–10.8 keV, 10.8–21.9 keV; hereafter labelled bands A, B, C, and D¹. Note that this is one fewer energy band and half the time resolution than for our Cyg X–1 observations (Nowak et al. 1998a). This was required to obtain good statistics because the GX 339–4 observations discussed here ranged from 200–800 cts s^{-1} , as opposed to the 4500 cts s^{-1} observed for Cyg X–1. Energy bands A–D each had roughly the same count rate for a given observation. As for the spectral analysis (paper I), we found that all the observations were similar in their properties, with the exception of Observation 5. Observation 5 was approximately a factor of 5 fainter than the brightest observation (Observation 1).

As for our RXTE observations of Cyg X–1 (Nowak et al. 1998a), we combined low frequency ($\approx 8 \times 10^{-4}$ – 7×10^{-3} Hz) FFTs made from a few (6–16) data segments of length 512–1024 s with higher frequency (7×10^{-3} –128 Hz) FFTs made from somewhat more ($\gtrsim 70$) data segments of length 128 s. From these data segments we created PSDs for all of our observations. We present two examples of the resulting PSDs in Figure 2. With the exception of Observation 5, all PSDs were qualitatively and quantitatively similar to that presented in Figure 2 for Observation 7. The PSDs for Observations 1–4 and 6–7 have shapes roughly similar to what we observed for Cyg X–1: flat from $\approx 10^{-3}$ –0.03 Hz, approximately $\propto f^{-1}$ in-between 0.03–3 Hz, and steeper above ≈ 3 Hz (Nowak et al. 1998a). The PSDs for Observation 5 have qualitatively similar shapes; however, the break frequencies are approximately a factor of three lower.

Doubly broken power laws provided adequate descriptions of the PSDs for our RXTE observations of Cyg X–1 (Nowak et al. 1998a). Here, however, we clearly see that the GX 339–4 PSDs contain more structure. An ≈ 0.3 Hz quasi-periodic oscillation (QPO) is evident in Observation 7. In fact, this QPO appears at some level in *all* of our observations *except* Observation 5. Even ignoring the QPO features, the PSD is only marginally approximated by a doubly broken power law.

We have tried to fit the shape of the PSDs with a number of different functional forms. For example, a singly broken power law with a Lorentzian *absorption* feature at ≈ 0.3 –1 Hz provides good fits to all of the PSDs. Here we show the results of fitting a weak power law plus two broad Lorentzians. As we further elaborate upon in §4 and §5, such a fit may have some physical relevance. The Lorentzian and power law components may represent separate, broad-band processes that are individually coherent (between their soft and hard variability), but that are incoherent with one another.

Sample fits to the broad-band power are presented in Figure 3, and results for all of our data are presented in Table 1. The functional form of the Lorentzians that we fit is given by

$$P(f) = \pi^{-1} \frac{R^2 Q f_0}{f_0^2 + Q^2 (f - f_0)^2} . \quad (1)$$

Here f_0 is the resonant frequency of the Lorentzian, Q is the quality factor ($\approx f_0/\Delta f$, where Δf is the full-width-half-

maximum of the Lorentzian), and R is the fit amplitude (root mean square variability, $\text{rms} = R[1/2 - \tan^{-1}(-Q)/\pi]^{1/2}$, i.e. $\text{rms} = R$ as $Q \rightarrow \infty$). For all the fits presented in Table 1, $Q \lesssim 1$. We thus cannot consider the broad-peaks in the observed PSDs to be “quasi-periodic oscillations”. The fits are more rightly considered to be indicative of broad-band power with characteristic timescales $\sim f_0^{-1}$. Note also that, for all of the fits, $\chi_{\text{red}}^2 \lesssim 2$ –3. Although this formally represents an unacceptable fit, this is partly attributable to the excellent statistics achievable with RXTE. Even small fractional deviations from the fit are highly statistically significant. In practice we have found that $\chi_{\text{red}}^2 \lesssim 2$ is nearly impossible to achieve with any simple functional fits. Furthermore, the fits with the largest χ_{red}^2 showed the most pronounced 0.3 Hz QPO, as in Observation 7.

For Observations 1–4 and 6–7, the low frequency broad-band power was peaked near ≈ 0.3 Hz, while the high frequency broad-band power was peaked near ≈ 2.5 Hz. The rms variability amplitudes were all comparable for these observations. Observation 5 had a somewhat larger rms variability amplitude. The trend for all observations was for the rms variability amplitude, measured from 7×10^{-3} –40 Hz, to decrease with increasing energy band, although this is only marginally evident in the individual fit components (cf. Figure 1). In Figure 1 we plot the best fit rms variabilities and peak frequencies for the two Lorentzian fit components vs. the observed 3–9 keV flux.

Observations 1–4 and 6–7 span a factor of two in observed 3–9 keV flux. The PSD parameters, however, show no obvious trends with flux, except for exhibiting weak evidence for the rms variability of the low frequency Lorentzian fit component to increase with 3–9 keV luminosity. Perhaps the most remarkable aspect of this subset of the observations is how similar all the PSDs appear to one another despite the factor of two spread in the observed 3–9 keV flux.

The ≈ 0.3 Hz QPO is most prominent in Observation 7. Its strength and width are somewhat difficult to characterize, however, as it is difficult to determine the ‘continuum’ level of the PSD to which it should be compared. The rise of the QPO appears sharper than its decline, and typically there is a PSD ‘dip’ at ≈ 0.05 Hz before the peak of the QPO. We have tried a variety of narrow Lorentzian plus broad-band power fits to the features; however, the best fit parameters are highly dependent upon the assumed form of the underlying broad-band PSD. Furthermore, narrow Lorentzian fits do not capture the asymmetric shape of the QPO.

Being unable to find a satisfactory functional fit to the QPO, we have chosen to characterize it in the following manner. We have measured the location of the PSD ‘dip’ that occurs before the QPO peak, as well as the location of the QPO peak. (Factoring in noise fluctuations, the QPO is sharp enough from dip to peak that the location of each is likely accurate to better than two unaveraged frequency bins, i.e. 0.015 Hz.) We have also measured the dip and peak PSD amplitudes. As for the fits to the broad-band PSD discussed above, there are no obvious trends between QPO parameters and the observed 3–9 keV flux. Furthermore, there is no obvious trend between QPO peak power and frequency, as shown in Figure 5. Although the QPO frequency is characteristically near 0.3 Hz, it is not at a steady frequency and it varies over a range of 0.08 Hz. Peak QPO amplitudes and widths, however, are somewhat less variable. Note that the *total* rms variability in the region of the QPO typically is $\approx 5\%$, therefore the QPO amplitude is at most a few percent.

¹We also created 2^{-13} s resolution lightcurves to search for signatures of high frequency features. No evidence for such features was found. Note also that the effective lower limit for energy band A is more ≈ 2 keV.

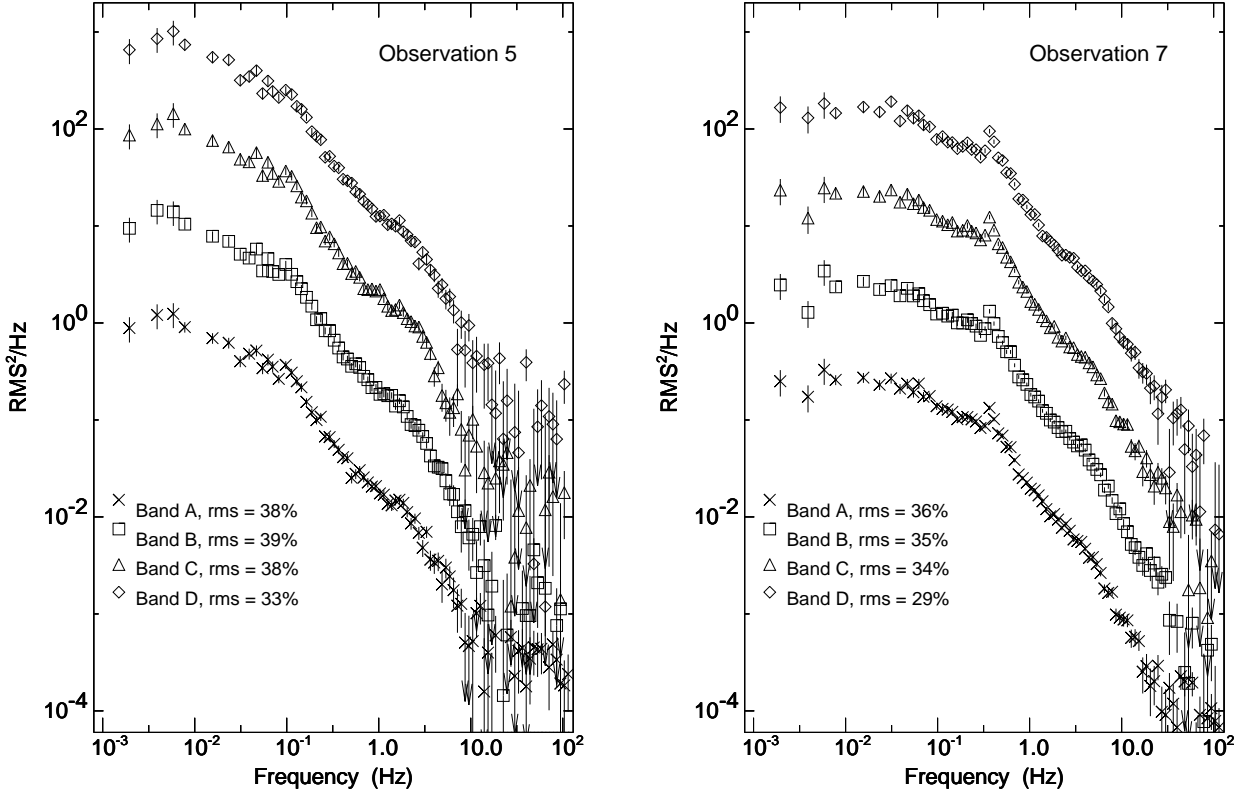


FIG. 2.— PSDs with associated uncertainties for Observation 5 (*left*) and for Observation 7 (*right*). All PSD are for the one-sided normalization of Belloni & Hasinger (1990b), where integrating over positive frequencies yields the total mean square variability. Crosses correspond to energy band A, squares to energy band B shifted upwards by a factor of 10, triangles to energy band C shifted upward by a factor of 100, and diamonds to energy band D shifted upward by a factor of 1000. (See text for the energy range of the bands.) Root mean square (rms) variability values were calculated between $f = 7 \times 10^{-3}$ –40 Hz.

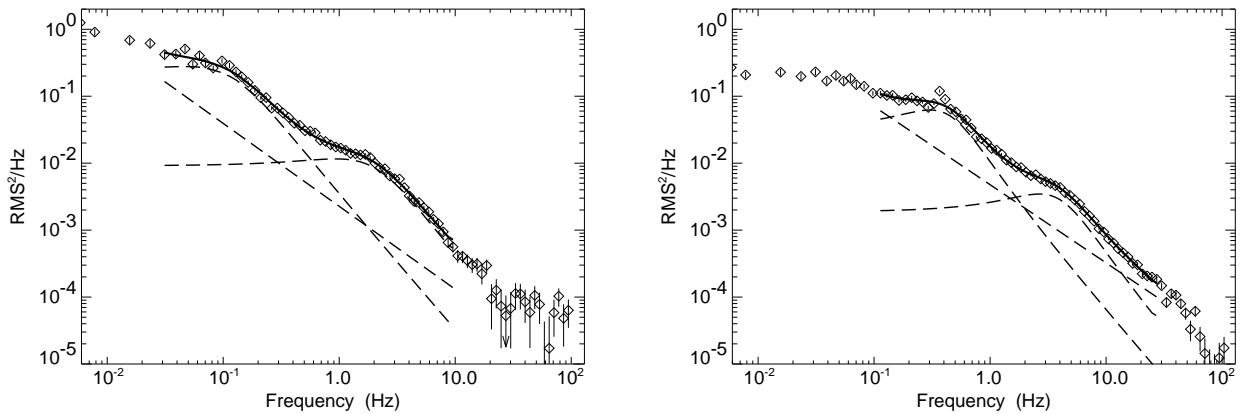


FIG. 3.— *Left*: Diamonds are the PSD for Observation 5 (energy bands A–D summed), normalized as in Belloni & Hasinger (1990b). *Right*: Diamonds are the PSD for Observation 7 (energy bands A–D summed). For both figures, the solid line is the best fit power law plus two broad Lorentzians. (Fit range is 0.03–10 Hz for Observation 5, and 0.1–30 Hz for Observation 7.) Dashed lines show the individual components of the fits.

TABLE 1

FITS TO THE PSD OF THE FORM: $Af^\Gamma + \pi^{-1} (R_1^2 Q_1 f_1 / [f_1^2 + Q_1^2 (f - f_1)^2] + R_2^2 Q_2 f_2 / [f_2^2 + Q_2^2 (f - f_2)^2])$. ENERGY RANGES OF BANDS A–D ARE DESCRIBED IN THE TEXT. T REPRESENTS ENERGY BANDS A–D SUMMED TOGETHER. ALL FITS WERE IN THE RANGE $f = 0.1\text{--}30\text{ Hz}$ (47 DEGREES OF FREEDOM), EXCEPT FOR OBSERVATION 5 WHICH WAS FIT IN THE RANGE $f = 0.03\text{--}10\text{ Hz}$ (45 DEGREES OF FREEDOM).

ERRORS ARE THE NOMINAL 90% CONFIDENCE LEVEL FOR ONE INTERESTING PARAMETER ($\Delta\chi^2 = 2.71$).

Obs.	Band	R_1 ($\times 10^{-2}$)	f_1 (Hz)	Q_1	A ($\times 10^{-3}$)	Γ	R_2 ($\times 10^{-2}$)	f_2 (Hz)	Q_2	χ^2
1	A	24^{+2}_{-2}	$0.33^{+0.04}_{-0.04}$	$1.2^{+0.3}_{-0.2}$	$7.5^{+1.4}_{-1.7}$	$-1.23^{+0.06}_{-0.11}$	19^{+3}_{-2}	$2.2^{+0.3}_{-0.6}$	$0.9^{+0.2}_{-0.3}$	102.
1	B	26^{+2}_{-2}	$0.31^{+0.04}_{-0.03}$	$1.0^{+0.3}_{-0.2}$	$5.4^{+1.4}_{-1.8}$	$-1.28^{+0.07}_{-0.18}$	21^{+3}_{-2}	$2.6^{+0.3}_{-0.6}$	$0.8^{+0.2}_{-0.3}$	116.
1	C	25^{+2}_{-2}	$0.31^{+0.04}_{-0.03}$	$1.0^{+0.3}_{-0.2}$	$4.7^{+1.6}_{-2.5}$	$-1.26^{+0.08}_{-0.32}$	21^{+4}_{-2}	$2.4^{+0.4}_{-0.8}$	$0.7^{+0.2}_{-0.3}$	84.
1	D	20^{+1}_{-2}	$0.35^{+0.03}_{-0.02}$	$1.3^{+0.3}_{-0.2}$	$5.6^{+1.0}_{-1.1}$	$-1.17^{+0.04}_{-0.09}$	16^{+3}_{-2}	$3.2^{+0.3}_{-0.6}$	$1.1^{+0.2}_{-0.4}$	112.
1	T	25^{+2}_{-2}	$0.30^{+0.04}_{-0.03}$	$0.9^{+0.3}_{-0.1}$	$5.7^{+0.9}_{-0.9}$	$-1.19^{+0.04}_{-0.06}$	18^{+1}_{-1}	$2.9^{+0.1}_{-0.3}$	$1.1^{+0.1}_{-0.2}$	129.
2	A	27^{+3}_{-4}	$0.28^{+0.06}_{-0.03}$	$0.9^{+0.4}_{-0.1}$	$4.6^{+2.7}_{-3.4}$	$-1.46^{+0.13}_{-0.51}$	23^{+4}_{-3}	$2.2^{+0.4}_{-0.7}$	$0.8^{+0.3}_{-0.2}$	103.
2	B	26^{+2}_{-3}	$0.29^{+0.05}_{-0.03}$	$0.9^{+0.3}_{-0.1}$	$6.3^{+1.8}_{-1.7}$	$-1.30^{+0.08}_{-0.15}$	20^{+3}_{-2}	$2.6^{+0.3}_{-0.5}$	$0.9^{+0.2}_{-0.3}$	73.
2	C	22^{+2}_{-3}	$0.32^{+0.04}_{-0.03}$	$1.3^{+0.4}_{-0.2}$	$6.7^{+1.8}_{-2.9}$	$-1.27^{+0.08}_{-0.23}$	21^{+4}_{-3}	$2.2^{+0.5}_{-1.0}$	$0.7^{+0.3}_{-0.4}$	74.
2	D	21^{+3}_{-3}	$0.31^{+0.04}_{-0.03}$	$1.1^{+0.4}_{-0.2}$	$3.7^{+2.0}_{-3.4}$	$-1.35^{+0.13}_{-0.62}$	20^{+3}_{-3}	$2.2^{+0.4}_{-0.7}$	$0.6^{+0.3}_{-0.3}$	94.
2	T	25^{+2}_{-3}	$0.28^{+0.05}_{-0.03}$	$0.9^{+0.3}_{-0.1}$	$6.1^{+1.1}_{-0.9}$	$-1.24^{+0.04}_{-0.06}$	18^{+1}_{-1}	$2.8^{+0.1}_{-0.3}$	$1.0^{+0.1}_{-0.2}$	102.
3	A	24^{+3}_{-3}	$0.32^{+0.03}_{-0.03}$	$1.3^{+0.4}_{-0.2}$	$4.6^{+2.8}_{-2.9}$	$-1.46^{+0.16}_{-0.51}$	24^{+3}_{-4}	$1.8^{+0.5}_{-0.3}$	$0.6^{+0.3}_{-0.1}$	77.
3	B	25^{+2}_{-2}	$0.30^{+0.04}_{-0.03}$	$1.1^{+0.3}_{-0.2}$	$5.3^{+1.8}_{-1.6}$	$-1.32^{+0.09}_{-0.16}$	22^{+3}_{-2}	$2.2^{+0.3}_{-0.4}$	$0.8^{+0.2}_{-0.2}$	86.
3	C	22^{+2}_{-2}	$0.32^{+0.03}_{-0.02}$	$1.3^{+0.4}_{-0.2}$	$5.9^{+1.7}_{-3.4}$	$-1.27^{+0.06}_{-0.38}$	22^{+3}_{-2}	$2.0^{+0.4}_{-0.4}$	$0.6^{+0.3}_{-0.3}$	73.
3	D	19^{+1}_{-2}	$0.35^{+0.02}_{-0.02}$	$1.5^{+0.3}_{-0.2}$	$5.0^{+1.3}_{-2.7}$	$-1.25^{+0.08}_{-0.33}$	19^{+3}_{-2}	$2.2^{+0.4}_{-0.4}$	$0.7^{+0.3}_{-0.3}$	92.
3	T	24^{+1}_{-3}	$0.30^{+0.04}_{-0.02}$	$1.1^{+0.3}_{-0.1}$	$5.4^{+1.0}_{-0.8}$	$-1.26^{+0.03}_{-0.08}$	20^{+2}_{-1}	$2.5^{+0.1}_{-0.4}$	$0.9^{+0.1}_{-0.2}$	119.
4	A	19^{+2}_{-3}	$0.35^{+0.03}_{-0.03}$	$1.6^{+0.7}_{-0.4}$	$11.5^{+1.8}_{-2.1}$	$-1.17^{+0.05}_{-0.09}$	16^{+5}_{-3}	$2.0^{+0.5}_{-0.7}$	$0.9^{+0.5}_{-0.3}$	48.
4	B	24^{+2}_{-3}	$0.31^{+0.05}_{-0.04}$	$1.1^{+0.5}_{-0.2}$	$6.3^{+2.1}_{-4.5}$	$-1.30^{+0.09}_{-0.53}$	20^{+4}_{-3}	$2.4^{+0.4}_{-1.1}$	$0.8^{+0.3}_{-0.4}$	82.
4	C	19^{+2}_{-2}	$0.36^{+0.03}_{-0.03}$	$1.5^{+0.5}_{-0.3}$	$7.5^{+2.1}_{-5.0}$	$-1.24^{+0.07}_{-0.47}$	21^{+7}_{-4}	$1.9^{+0.8}_{-1.5}$	$0.6^{+0.4}_{-0.5}$	62.
4	D	17^{+2}_{-2}	$0.37^{+0.03}_{-0.03}$	$1.5^{+0.5}_{-0.3}$	$6.8^{+1.3}_{-1.4}$	$-1.16^{+0.05}_{-0.10}$	14^{+4}_{-2}	$3.0^{+0.4}_{-0.8}$	$1.2^{+0.5}_{-0.5}$	66.
4	T	22^{+2}_{-3}	$0.31^{+0.05}_{-0.03}$	$1.0^{+0.4}_{-0.2}$	$6.5^{+1.1}_{-0.9}$	$-1.23^{+0.04}_{-0.07}$	18^{+2}_{-1}	$2.7^{+0.2}_{-0.5}$	$1.0^{+0.1}_{-0.2}$	86.
5	A	27^{+12}_{-8}	$0.08^{+0.04}_{-0.05}$	$0.8^{+1.0}_{-0.6}$	$5.1^{+6.5}_{-4.8}$	$-1.11^{+0.06}_{-0.85}$	25^{+7}_{-10}	$1.0^{+0.7}_{-0.7}$	$0.6^{+1.1}_{-0.4}$	59.
5	B	31^{+9}_{-7}	$0.07^{+0.04}_{-0.05}$	$0.6^{+0.6}_{-0.5}$	$3.5^{+5.0}_{-3.2}$	$-1.23^{+0.92}_{-0.73}$	29^{+4}_{-7}	$0.7^{+0.5}_{-0.4}$	$0.4^{+0.5}_{-0.2}$	46.
5	C	35^{+8}_{-10}	$0.04^{+0.05}_{-0.04}$	$0.4^{+0.7}_{-0.3}$	$1.6^{+5.1}_{-1.4}$	$-1.30^{+1.10}_{-0.67}$	28^{+4}_{-5}	$1.0^{+0.4}_{-0.6}$	$0.6^{+0.3}_{-0.3}$	69.
5	D	23^{+7}_{-7}	$0.08^{+0.04}_{-0.03}$	$0.8^{+0.8}_{-0.3}$	$5.0^{+4.0}_{-3.8}$	$-1.07^{+0.19}_{-0.41}$	20^{+7}_{-8}	$1.1^{+0.6}_{-0.6}$	$0.6^{+0.9}_{-0.4}$	49.
5	T	35^{+5}_{-8}	$0.03^{+0.04}_{-0.03}$	$0.3^{+0.4}_{-0.2}$	$1.0^{+3.2}_{-0.4}$	$-1.25^{+0.60}_{-0.45}$	27^{+2}_{-4}	$0.9^{+0.3}_{-0.3}$	$0.5^{+0.2}_{-0.2}$	85.
6	A	21^{+2}_{-3}	$0.33^{+0.04}_{-0.03}$	$1.4^{+0.6}_{-0.2}$	$9.6^{+1.7}_{-1.5}$	$-1.17^{+0.04}_{-0.09}$	17^{+4}_{-2}	$2.4^{+0.3}_{-0.6}$	$1.2^{+0.4}_{-0.5}$	83.
6	B	25^{+2}_{-3}	$0.29^{+0.05}_{-0.03}$	$1.1^{+0.4}_{-0.2}$	$6.6^{+1.7}_{-1.4}$	$-1.18^{+0.06}_{-0.10}$	18^{+3}_{-2}	$2.7^{+0.2}_{-0.4}$	$1.1^{+0.2}_{-0.3}$	89.
6	C	22^{+3}_{-3}	$0.33^{+0.04}_{-0.02}$	$1.3^{+0.5}_{-0.2}$	$5.3^{+2.1}_{-4.1}$	$-1.31^{+0.10}_{-0.65}$	22^{+4}_{-3}	$2.0^{+0.5}_{-1.1}$	$0.7^{+0.3}_{-0.4}$	72.
6	D	18^{+2}_{-2}	$0.34^{+0.03}_{-0.02}$	$1.5^{+0.5}_{-0.2}$	$4.7^{+1.7}_{-3.1}$	$-1.26^{+0.09}_{-0.51}$	20^{+5}_{-3}	$1.9^{+0.6}_{-1.5}$	$0.6^{+0.3}_{-0.4}$	75.
6	T	23^{+1}_{-3}	$0.30^{+0.05}_{-0.02}$	$1.1^{+0.4}_{-0.1}$	$5.8^{+1.1}_{-0.8}$	$-1.21^{+0.04}_{-0.07}$	19^{+2}_{-1}	$2.6^{+0.1}_{-0.3}$	$1.0^{+0.1}_{-0.2}$	101.
7	A	22^{+2}_{-2}	$0.38^{+0.03}_{-0.02}$	$1.7^{+0.4}_{-0.3}$	$4.6^{+2.5}_{-2.8}$	$-1.45^{+0.18}_{-0.37}$	28^{+2}_{-4}	$0.8^{+0.7}_{-0.3}$	$0.3^{+0.3}_{-0.1}$	115.
7	B	24^{+1}_{-2}	$0.36^{+0.03}_{-0.02}$	$1.3^{+0.4}_{-0.3}$	$6.2^{+1.4}_{-1.8}$	$-1.22^{+0.06}_{-0.16}$	21^{+2}_{-2}	$2.1^{+0.6}_{-0.5}$	$0.7^{+0.4}_{-0.3}$	115.
7	C	23^{+1}_{-2}	$0.36^{+0.04}_{-0.03}$	$1.3^{+0.4}_{-0.2}$	$6.1^{+1.3}_{-2.1}$	$-1.15^{+0.06}_{-0.20}$	19^{+3}_{-2}	$2.4^{+0.5}_{-1.6}$	$0.7^{+0.3}_{-0.5}$	112.
7	D	20^{+1}_{-2}	$0.39^{+0.03}_{-0.02}$	$1.4^{+0.4}_{-0.2}$	$4.8^{+0.7}_{-2.2}$	$-1.14^{+0.04}_{-0.24}$	16^{+3}_{-1}	$2.7^{+0.3}_{-1.5}$	$0.8^{+0.2}_{-0.5}$	124.
7	T	25^{+1}_{-2}	$0.33^{+0.04}_{-0.03}$	$1.0^{+0.2}_{-0.1}$	$4.9^{+0.7}_{-0.8}$	$-1.18^{+0.05}_{-0.06}$	19^{+1}_{-1}	$2.7^{+0.2}_{-0.3}$	$0.9^{+0.1}_{-0.1}$	165.
8	A	21^{+2}_{-2}	$0.36^{+0.04}_{-0.05}$	$1.3^{+0.3}_{-0.3}$	$9.7^{+1.5}_{-1.8}$	$-1.20^{+0.05}_{-0.08}$	16^{+2}_{-3}	$2.7^{+0.3}_{-0.5}$	$1.2^{+0.5}_{-0.4}$	61.
8	B	23^{+5}_{-2}	$0.36^{+0.03}_{-0.05}$	$1.2^{+0.3}_{-0.3}$	$5.1^{+2.2}_{-3.9}$	$-1.45^{+0.15}_{-0.69}$	23^{+4}_{-4}	$1.9^{+0.6}_{-0.7}$	$0.6^{+0.3}_{-0.2}$	78.
8	C	21^{+5}_{-2}	$0.36^{+0.03}_{-0.06}$	$1.2^{+0.3}_{-0.3}$	$5.0^{+2.4}_{-3.7}$	$-1.42^{+0.15}_{-0.71}$	23^{+5}_{-4}	$1.8^{+0.8}_{-1.1}$	$0.5^{+0.4}_{-0.3}$	78.
8	D	18^{+4}_{-2}	$0.37^{+0.03}_{-0.05}$	$1.3^{+0.3}_{-0.4}$	$3.9^{+2.0}_{-2.8}$	$-1.37^{+0.17}_{-0.60}$	22^{+4}_{-5}	$1.1^{+1.2}_{-0.6}$	$0.3^{+0.4}_{-0.2}$	67.
8	T	21^{+2}_{-1}	$0.35^{+0.03}_{-0.03}$	$1.1^{+0.2}_{-0.2}$	$5.7^{+0.8}_{-1.0}$	$-1.33^{+0.05}_{-0.07}$	20^{+2}_{-1}	$2.3^{+0.3}_{-0.3}$	$0.7^{+0.1}_{-0.1}$	74.

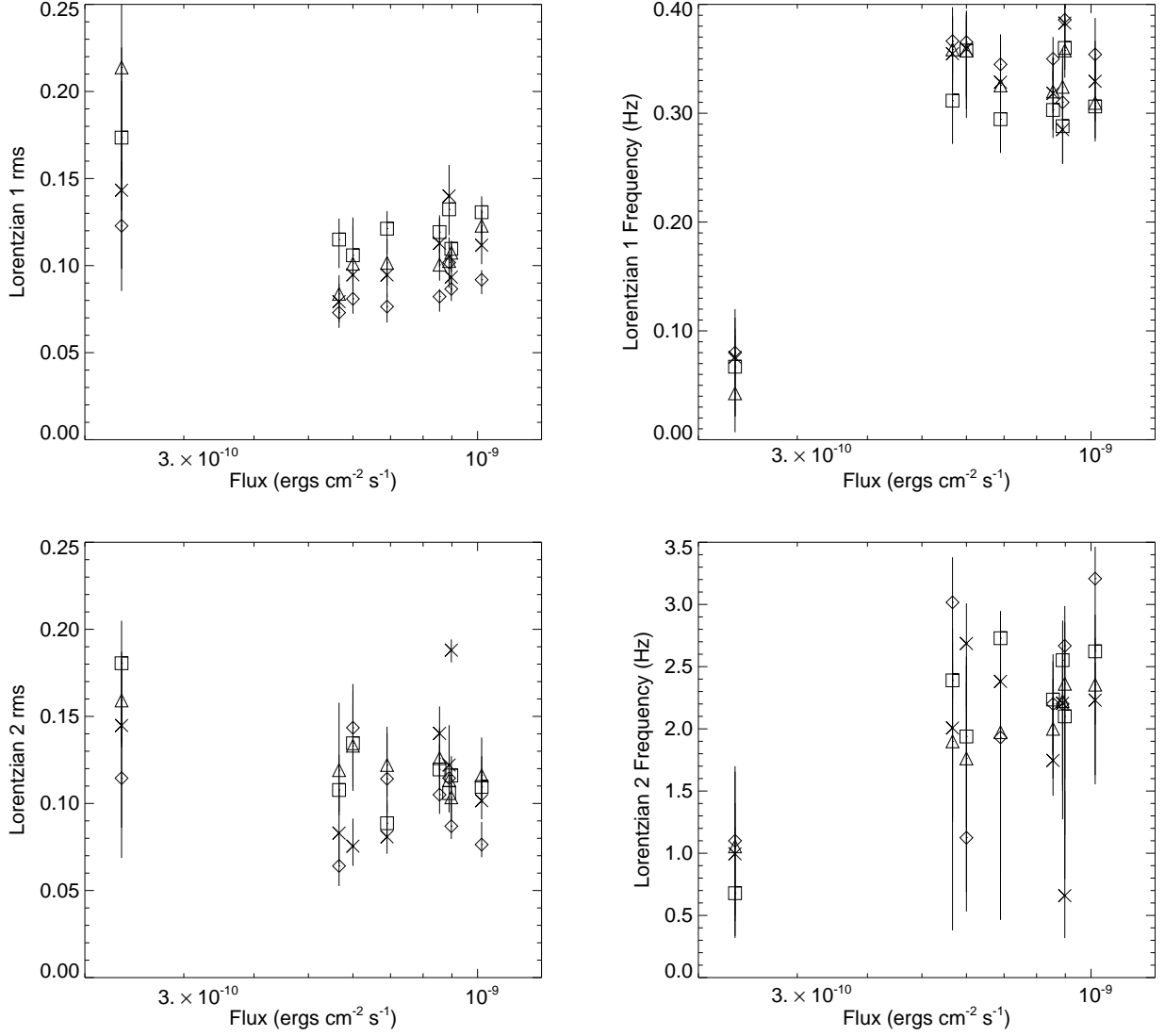


FIG. 4.— *Upper Left:* rms variability of the low-frequency broad Lorentzian fit component vs. the 3–9 keV flux of the observation. *Upper Right:* Peak frequency of the low-frequency broad Lorentzian fit component vs. the 3–9 keV flux of the observation. *Lower Left:* rms variability of the high-frequency broad Lorentzian fit component vs. the 3–9 keV flux of the observation. *Lower Right:* Peak frequency of the high-frequency broad Lorentzian fit component vs. the 3–9 keV flux of the observation. Symbols are the same as for Figure 2.

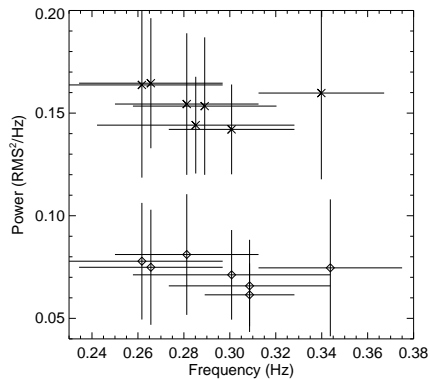


FIG. 5.— QPO PSD amplitude vs. frequency. The bars extend from the values for the dip to the values of the peak (see text), and the points are placed at the midpoint. Crosses are for energy band A and diamonds are for energy band D, with PSD amplitude lowered by 0.1.

4. COHERENCE AND TIME LAGS

As discussed by Vaughan & Nowak (1997), the coherence function is a measure of the degree of linear correlation between two time series. Specifically, it gives the fraction of the mean-squared variability at a given Fourier frequency in one time series that can be attributed to, or equivalently predicted from, the other. The fact that coherence is often near unity over a wide range of frequencies (cf. Vaughan & Nowak 1997; Nowak et al. 1998a) is what makes it meaningful to then talk about characteristic Fourier frequency-dependent time delays between two time series (cf. Miyamoto & Kitamoto 1989; Miyamoto et al. 1992; van der Klis 1989; Nowak et al. 1998a).

The techniques that we used to calculate the coherence and time delays for the GX 339–4 lightcurves are discussed in Vaughan & Nowak (1997) and Nowak et al. (1998a). For all observations we have calculated the coherence function,

$$\gamma^2(f) = \frac{|\langle S^*(f)H(f) \rangle|^2}{\langle |S(f)|^2 \rangle \langle |H(f)|^2 \rangle}, \quad (2)$$

between the FFTs for energy band A [$S(f)$] and the FFTs for the other three energy bands [$H(f)$], angle brackets indicating averages over Fourier frequencies and individual data segments; cf. Vaughan & Nowak 1997; Nowak et al. 1998a]. For all observations except for Observation 5, we have calculated the time-delay between energy band A and the other three energy-bands. For Observation 5, noise limitations only allow us to calculate the time-delay between the lightcurves for energy band D and energy band A. We have averaged over logarithmically spaced frequency bins, ranging over frequencies $f \rightarrow 1.4f$ for all observations.

As shown in Figure 6, the coherence function is near unity from 10^{-3} to ≈ 3 Hz (Observation 5) or ≈ 10 Hz (all other observations). Above ≈ 3 – 10 Hz, there is a noticeable drop in coherence, similar to what we saw with our RXTE observations of Cyg X–1 (Nowak et al. 1998a). The Cyg X–1 observations also showed a loss of coherence below ≈ 0.02 Hz; however, the coherence in GX 339–4 remains near unity down to Fourier frequencies as low as $\approx 10^{-3}$ Hz.

We note that the coherence between energy bands A and D shows evidence of an ≈ 0.1 dip near 0.5 Hz (Observation 5) and near 2 Hz (all other observations). The evidence for this dip is weak in Observation 5 (comparing band A to D, the 0.45 Hz point is 2σ below unity, and the adjacent 0.64 Hz point is only 1σ below unity), but is somewhat stronger for Observation 7 and the other observations (comparing band A to D for Observation 7, the 1.8 Hz point is $> 3\sigma$ below unity, and the adjacent 2.5 Hz point is $\approx 2.7\sigma$ below unity). These dip frequencies, however, are approximately the frequencies at which the two broad Lorentzian and power law fit components (cf. Figure 3 and Tab. 1) overlap. Thus we hypothesize that there are indeed multiple broad-band processes occurring in GX 339–4 that are individually coherent but that are incoherent with one another. As with Cygnus X–1, we further hypothesize that the loss of coherence at high-frequency is indicative of multiple incoherent processes, possibly ‘flares’ feeding the corona on dynamical timescales (Nowak et al. 1998a; Nowak et al. 1998b).

In Figure 6 we also show the energy-dependent and Fourier frequency-dependent time delays. The overall structure is very similar to that observed in the hard state of Cyg X–1 (Miyamoto & Kitamoto 1989; Miyamoto et al. 1992; Cray et al. 1998; Nowak et al. 1998a). In the regions not dominated by noise statistics, the hard photon variability always lags the soft pho-

ton variability, and the delays decrease with increasing Fourier frequency. The detailed frequency-dependent structure of the delays, however, is more complicated than a simple power law. For example, the time lags between bands A and D for Observation 7 show a flattened region near 1 Hz. As for Cyg X–1, there is a large dynamic range in the time delays, with the longest time delays (≈ 0.1 s) being much longer than typical characteristic timescales of a small corona (cf. Nowak et al. 1998b). Also as has been observed for Cyg X–1 (Miyamoto & Kitamoto 1989; Miyamoto et al. 1992; Cray et al. 1998; Nowak et al. 1998a), the time delay observed in GX 339–4 is consistent with scaling as the logarithm of the ratio of the two energies being compared. This latter fact has prompted Kazanas, Hua & Titarchuk (1997) (hereafter KHT) to suggest that the time-delays are related to photon propagation timescales in a very large ($R \approx 10^5 GM/c^2$) corona. In Figure 7 we show the measured time delay for three Fourier frequencies (0.1 Hz, 0.9 Hz, 2.5 Hz) as a function of the measured 3–9 keV flux. The lowest flux observation consistently shows the shortest time delays at nearly all Fourier frequencies. The highest flux observation shows the longest time delays at many Fourier frequencies, and shows at least the second longest time delays at nearly all Fourier frequencies. Observations at intermediate fluxes are scattered both positively and negatively about an extrapolation between the low- and high-flux point. It has been previously shown that the time delay decreases in Cyg X–1 as it transits from the hard to soft state (cf. Cui et al. 1997). Here we present a possible correlation between the magnitude of the time delay and the energy flux for the hard state within a single source. The strong decrease of the time delay for the lowest flux observation is counter to the simplest expectations if the coronal size increases with decreasing flux (e.g. Esin, McClintock & Narayan 1997), or if characteristic ‘propagation speeds’ in the corona decrease with decreasing luminosity (Nowak et al. 1998b). However, if the coronal size is decreasing with decreasing luminosity then this observed decrease is understandable in terms of propagation models, whether it be propagation of photons (KHT) or propagation of some sort of other disturbance (Nowak et al. 1998b).

We have found one potential correlation between the measured time lags and the coherence function, related to the vector analogy for the phase lags and coherence function discussed by Nowak et al. (1998a). If we take the Fourier transform of a soft X-ray lightcurve, $A_s(f)$, and a Fourier transform for the hard X-ray lightcurve, $A_h(f)$, the cross spectrum is given by $A_s^*(f)A_h(f)$, which can be considered as a vector in the complex plane (cf. Fig. 8). As discussed by Vaughan & Nowak (1997), the magnitude and angle (corresponding to the phase delay between hard and soft variability) of this vector is well-defined if the coherence function is unity.

If the net observed cross spectrum, however, is made up of the sum of individually coherent processes, it is possible that the net observed coherence will be *less* than unity. As was noted by Vaughan & Nowak (1997), specifically eq. (10), a sum of individually coherent processes is itself coherent if and only if each process has the same identical transfer function from soft to hard photon variability. In terms of the vector analogy, this is a statement that the vectors representing each process within the sum all lie in the same direction. The coherence function in such a case is the square of the ratio of the magnitude of this sum compared to the magnitude of the sum if all the vectors had the same angle.

Let us consider the following special case of eq. (10) from

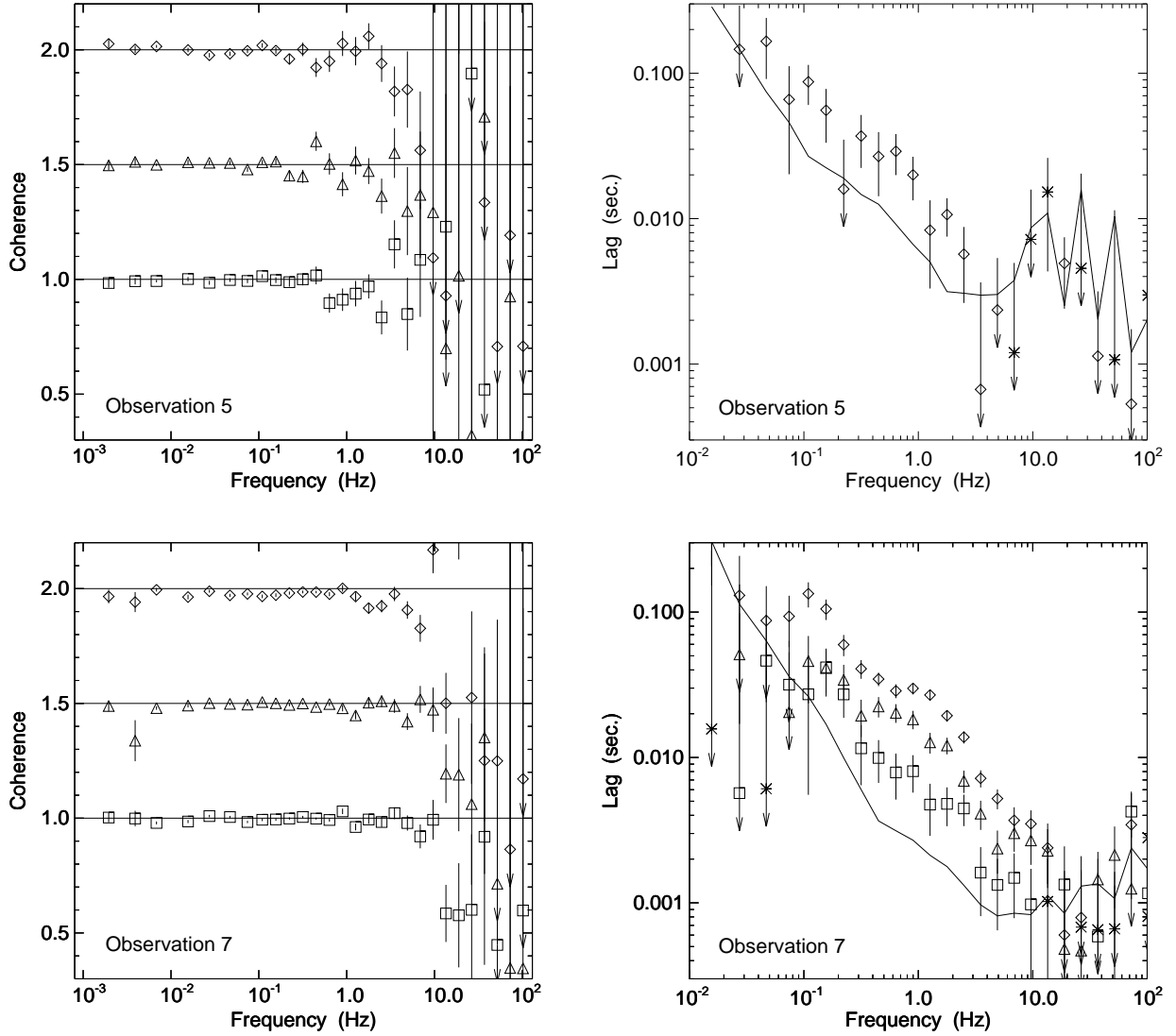


FIG. 6.— Coherence function and time lags of various energy channels [squares: channel B, triangles: channel C (coherence offset by 0.5), diamonds: channel D (coherence offset by 1.0)] as compared to energy channel A. *Top Left:* Coherence for Observation 5. Solid lines correspond to unity coherence. *Top Right:* Time lags for Observation 5. Crosses are where the soft variability lags the hard variability. Solid line is the Poisson noise level for channel D time lags. *Bottom Left:* Coherence for Observation 7. Solid lines correspond to unity coherence. *Bottom Right:* Time lags for Observation 7. Crosses are where the soft variability lags the hard variability. Solid line is the Poisson noise level for channel D time lags.

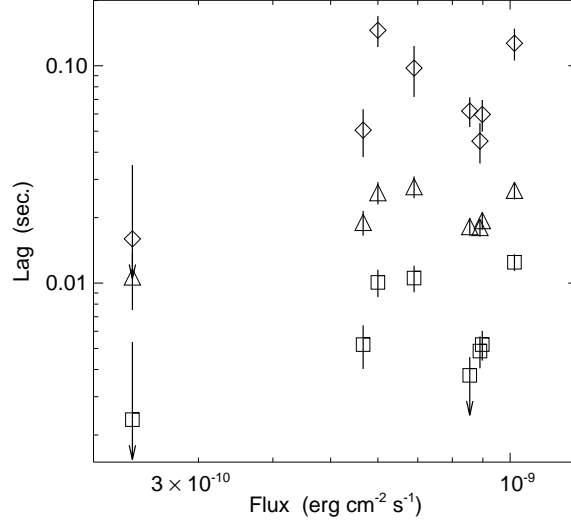


FIG. 7.— Time lags at Fourier frequencies 0.1 Hz (diamonds), 0.9 Hz (triangles), and 2.5 Hz (squares) as a function of measured 3–9 keV flux.

Vaughan & Nowak (1997). Assume that there are multiple input (soft) processes, indexed by i , with Fourier amplitudes $A_s^i(f)$. Let us assume that *each* of these input processes leads to an output process with Fourier amplitude $A_h^i(f)$ that has a *coherent* phase delay of $\Delta\phi_i(f)$. (Here we take the Fourier amplitudes to be real quantities.) Finally, assume that the input processes are incoherent with one another, and likewise that the output processes are incoherent with one another. Generalizing eq. (10) of Vaughan & Nowak (1997), the resulting measured coherence function will then be

$$\gamma_m^2(f) \approx \left(\sum_i A_s^{i2} A_h^{i2} + \sum_{i \neq j} A_s^i A_h^i A_s^j A_h^j \left[1 - \frac{(\Delta\phi_j - \Delta\phi_i)^2}{2} \right] \right) \times \left(\sum_i A_s^{i2} \sum_j A_h^{j2} \right)^{-1} \quad (3)$$

where we have adopted a small angle approximation. Under the same assumptions, the net measured phase lag will be given by

$$\Delta\phi_m(f) \approx \frac{\sum_i A_s^i A_h^i \Delta\phi_i}{\sum_i A_s^i A_h^i} \quad (4)$$

That is, the measured phase lag is simply the weighted mean of the individual phase lags. We illustrate this situation in Fig. 8. For such a model as this, the net observed phase delay is related to the net observed coherence function, and both in turn are related to the observed soft and hard PSDs. Fit parameters are the amplitudes (A_s^i, A_h^i) of the individual components of the soft and hard PSDs, and the phase lags ($\Delta\phi_i$) between the soft and hard variability for each of these components.

We have searched for such a connection between the Fourier phase lag and the coherence function by applying equations (3) and (4) to the data. We have assumed that there are three components to the PSD: a low and high frequency Lorentzian and a power law, as for the fits presented in Table 1. In the fitting procedure we assumed that all three $\Delta\phi_i(f)$ were independent of Fourier frequency. We refit the PSD data simultaneously while

fitting the phase lag and coherence data. We searched for the minimum of the sum of the χ^2 from the four data sets being fit: soft X-ray PSD, hard X-ray PSD, phase lags, and coherence. We fit the PSDs over the same frequency range and with the same frequency binning as in Table 1; however, we only fit the coherence and phase lags over the range $f = 0.2$ –4 Hz. This was the frequency range over which the phase lags were least affected by Poisson noise, *and* it avoided the strong loss of coherence at high frequency. These strong high frequency coherence losses, as we discuss further below, may be due to nonlinear processes, rather than be due to the sum of linear processes (cf. Vaughan & Nowak 1997). The results for these fits are presented in Figure 9 and in Table 2.

Assuming that the PSD, phase lags, and coherence are the result of summing three independent processes (a power-law plus two Lorentzians), we see that equations (3) and (4) seem to provide a rough description of the time lag and coherence data. The fits make plausible that there is indeed a deeper underlying connection between the time lag and coherence data. One feature of these fits is notable. Namely, in order to produce coherence drops as large as are seen, one needs to add linear processes with greatly varying intrinsic time lags. In fact, one process, the power law, has nearly no time delay between soft and hard variability, whereas the high frequency Lorentzian process is seen to require even intrinsically longer time lags than the already very long time lags that are measured.

5. DISCUSSION

Let us consider these results in light of two models: the Comptonization model of KHT and ‘shot noise’ models (cf., Terrell 1972; Sutherland, Weisskopf & Kahn 1978; Friedhorsky et al. 1979; Miyamoto & Kitamoto 1989; Lochner, Swank & Szymkowiak 1991; Nowak 1994, hereafter N94; Belloni et al. 1997; Poutanen & Fabian 1998, hereafter PF; and references therein). In the former model, a source of white noise is assumed to be present at the center of the system, which is then “filtered” by passage through a Compton corona. The PSD is attenuated on those timescales that are *shorter* than the characteristic diffusion timescales through the corona. Therefore,

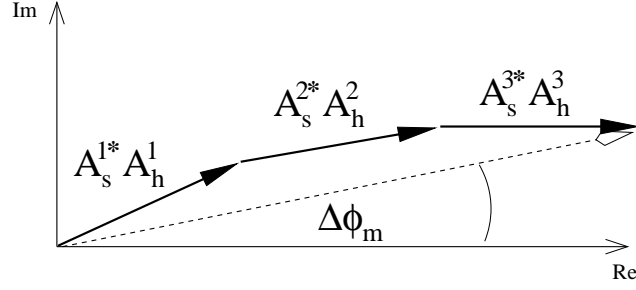


FIG. 8.— Vector analogy for phase lags and coherence. Cross power spectra ($A_s^{1*} A_h^1$, $A_s^{2*} A_h^2$, $A_s^{3*} A_h^3$) can be considered as vectors in the complex plane. The observed phase lag, $\Delta\phi_m$, is the angle of the vector sum of the individual components of the cross power spectrum. The coherence function is the square of the ratio of the magnitude of this sum compared to the magnitude of the sum if all the vectors had the same direction.

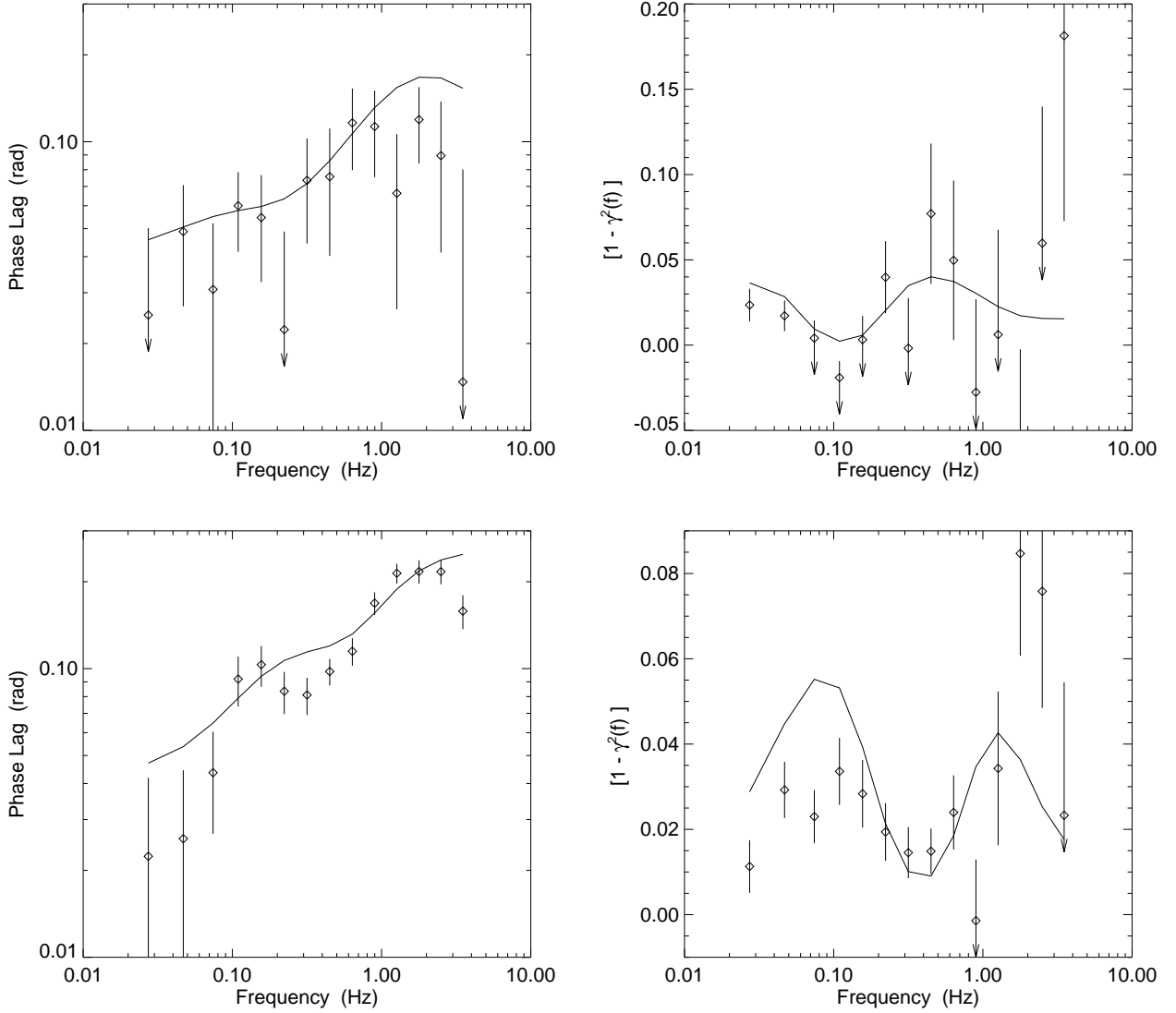


FIG. 9.— *Left:* Phase lags between energy band A and D as a function of Fourier frequency for Observation 5 (top) and Observation 7 (bottom). (All points are hard variability lagging soft variability.) *Right:* $[1 - \gamma_m^2(f)]$, where $\gamma_m^2(f)$ is the measured, noise subtracted coherence function between energy band A and D for Observation 5 (top) and Observation 7 (bottom). All data has been logarithmically binned over frequencies $f \rightarrow 1.4 f$. Solid lines are the best fit results for fitting equations of the form of eq. (2) and eq. (3) (see text and Table 2 for further explanation).

TABLE 2

BEST FIT FOURIER PHASE LAGS BETWEEN ENERGY CHANNELS A AND D, WHERE WE HAVE USED EQUATIONS OF THE FORM OF EQ. (2) AND EQ. (3) AND WHERE WE HAVE ASSUMED THREE SEPARATE COMPONENTS TO THE SOFT AND HARD X-RAY PSD. PSD COMPONENTS ARE AS IN TABLE 1: A LOW FREQUENCY LORENTZIAN (*l1*), A POWER LAW (*pl*), AND A HIGH FREQUENCY LORENTZIAN (*l2*). PSD DATA, LOGARITHMICALLY BINNED OVER FREQUENCIES $f \rightarrow 1.1 f$, WERE INCLUDED IN THE FITTING PROCESS WITH THE RESULTING FIT PARAMETERS ALWAYS BEING WITHIN THE ERROR BARS SHOWN IN TABLE 1. PHASES— $\Delta\phi_{l1}$, $\Delta\phi_{pl}$, $\Delta\phi_{l2}$ — ARE THE FOURIER PHASE LAGS BETWEEN HARD AND SOFT VARIABILITY FOR EACH PSD FIT COMPONENT INDIVIDUALLY, AND POSITIVE PHASE CORRESPONDS TO HARD VARIABILITY LAGGING BEHIND SOFT VARIABILITY. THE PHASE LAGS WERE ASSUMED TO BE CONSTANT AS A FUNCTION OF FOURIER FREQUENCY.

Obs.	$\Delta\phi_{l1}$ (rad)	$\Delta\phi_{pl}$ (rad)	$\Delta\phi_{l2}$ (rad)	χ^2/DoF	χ^2_{red}
1	0.13	0.06	0.49	301.5/119	2.53
2	0.18	0.05	0.26	283.4/119	2.38
3	0.13	0.04	0.28	269.9/119	2.27
4	0.15	0.06	0.66	195.8/119	1.65
5	0.06	0.04	0.25	132.4/113	1.17
6	0.16	0.05	0.38	217.4/119	1.82
7	0.11	0.04	0.27	309.9/119	2.60
8	0.16	0.05	0.41	198.2/119	1.67

the PSD is more attenuated at higher frequencies than at lower frequencies, which leads to the characteristic power law PSDs that are observed in hard state BHC. Time delays are created by the difference in diffusion times through the corona for hard and soft photons. Photons that scatter over large radii will have their intrinsic high frequency variability wiped out; therefore, any observed high frequency variability must be due to photons that scattered over short path lengths. High frequency variability thus exhibits short time delays between hard and soft photon variability. Low frequency variability potentially can be observed from photons that have scattered over large path lengths, and thus it can exhibit longer time delays between hard and soft variability. Extremely large coronal sizes of $\mathcal{O}(10^5 GM/c^2)$ are required to produce the longest observed time lags.

In shot noise models the lightcurve is assumed to be composed of statistically distributed shots of (possibly) varying profiles (cf. Lochner, Swank & Szymkowiak 1991 for detailed references and applications to Cyg X-1). Shot and distribution parameters are fit to various moments and statistics of the observed lightcurves. Time delays between hard and soft variability are assumed to be due to differing shot profiles and/or shot distributions in different energy bands (cf. Miyamoto & Kitamoto 1989; N94; PF). Recently, PF have associated the energy dependent shots with the ‘energization’ of a corona, which was parameterized by a series of equilibrium models where the energy input to the corona was a function of time.

Does the data prefer one model over the other? The detailed structure of the PSD is likely to be more difficult to produce in the KHT model. Although the observed PSD can be modeled as a singly broken power law with an ‘absorption’ feature, it is difficult to imagine a Compton corona configuration that would act as such a ‘notch filter’. It is somewhat easier to imagine, however, two or more preferred shot durations in the distribution of shot timescales. A suitable distribution of shot timescales could easily reproduce the type of PSD fits presented in §3.

Can the flux dependence of the PSD be reproduced? This depends upon whether the coronal radius decreases or increases as the observed flux decreases. The former possibility can be consistent with our ‘sphere+disk’ corona fits to the spectral data

(paper I). The latter is more consistent with the ADAF models to the spectral data (paper I), as lower luminosity often implies a larger ‘transition radius’ to advective flow. The transition radius in the ADAF models is the radius at which the flow transits from being geometrically thin, optically thick, and radiatively efficient to being geometrically thick, optically thin, and radiatively inefficient. The larger this transition radius, the smaller the overall accretion efficiency (cf. Narayan 1996; Esin, McClintock & Narayan 1997). Lower luminosities can be associated with lower overall efficiencies. The dependence of the coronal radius on observed X-ray luminosity is less constrained for our ‘sphere+disk’ coronal models (Dove et al. 1997; paper I). Larger coronae, however, can produce larger observed X-ray fluxes in these models.

In the KHT model, the larger the corona the more attenuated the high frequency PSD will be. This will cause the PSD to apparently ‘shift’ towards lower frequency. Similarly, shot noise models usually associate the shot timescales with characteristic accretion flow timescales. What sets these timescales are usually not explicit in shot noise models; however, one expects the timescales to *increase* for larger coronae, consistent with the expectations of the ADAF models. That is, we expect to see the lower characteristic frequencies associated with the outer accretion flow. Associating a smaller corona with lower luminosity, as can be fitted within the context of ‘sphere+disk’ corona models, would lead to trends opposite of the observations.

What is the expected relation between the PSD and the observed time lags for these models? If the coronal size decreases with decreasing luminosity, then the KHT model agrees with the observations. The shorter scattering path lengths of a small corona will produce characteristically shorter lags between the hard and soft photon variability. The KHT model also correctly reproduces the observed logarithmic energy dependence of the time lags. However, it is difficult for the KHT model to reconcile the lower frequency PSDs *simultaneously* with shorter time lags. Predictions for shot noise models are more dependent upon the specifics of each model.

Energy dependent shots were first suggested by Miyamoto &

Kitamoto (1989) as the cause of the hard X-ray variability lags observed in Cyg X–1. This model contained eight input shot profiles (four shot durations in two energy bands), and did not relate the timescales to specific disk physics. The magnitude and frequency dependence of the hard X-ray lags are adjustable by changing the duration of the hard shots relative to the soft shots. In describing observations of the ‘very high state’ timing properties of GX 339–4, N94 related the shot durations to viscous and thermal instability timescales in an accretion disk. The shots considered in this work were also temperature dependent and became hotter as the shots progressed. This model reproduced the observed energy dependence of the lags, with the exception that it did not reproduce the 1.2–2.3 keV photon variability lagging behind the 2.3–4.6 keV photon variability. As discussed in N94 and Nowak et al. (1997), any shot model where the characteristic temperature or hardness of the shot smoothly increases as the shot rises will reproduce time lags qualitatively similar to those observed in Cyg X–1 and GX 339–4. In the model of PF, the shot timescales are not related to any specific accretion timescales; however, the time-dependent shot hardness is related to a series of equilibrium Compton coronae models. There is a one-to-one correspondance between the shot amplitude and its hardness in this model. The PF model correctly reproduces the magnitude and energy dependence of the observed time lags.

We expect the following qualitative behavior for the models of both N94 and PF. If we scale the shot duration to longer timescales, thereby shifting the PSD to lower frequencies, we also expect the timelags to *increase*, which is *contrary* to the observations. The only way to have a shot produce a lower frequency PSD *and* lead to shorter time lags is to alter the spectrum of the shot as well as lengthen its duration. Whereas we do see changes in flux from GX 339–4, we do not see large changes in the best fit spectral parameters such as optical depth or coronal temperature. The observed energy spectra do not leave much room for varying the spectra of the presumed shots in order to fit both the high frequency PSD/long time lag data and the low frequency PSD/short time lag data that are observed. (It is possible, however, for the relative contributions to the spectra from a ‘steady component’ and a ‘shot component’ vary in such a way that the average spectrum remains relatively unchanged. The rms amplitude of the PSD significantly increases for the faintest observation, and therefore its average spectrum *does* have a greater contribution from the shots.)

What is the expected coherence function for these various models? Both the KHT model and the PF model produce unity coherence, whereas the model of N94 produces coherence substantially less than unity (Nowak et al. 1997). The KHT model only considers static coronae, whereas the PF model uses the same exact linear Comptonization spectrum for each individual shot. We expect both of these situations to produce unity coherence. The N94 model assumes both a sum of different shot spectra *and* each shot represents a *nonlinear* transfer function from soft to hard variability (Nowak et al. 1997; Vaughan & Nowak 1997).

Similar to Cyg X–1, GX 339–4 was seen to have near unity coherence over a broad range of frequencies, with a rolloff at ≈ 3 –10 Hz. Unlike Cyg X–1 (Nowak et al. 1998a), however, there was no evidence for a loss of coherence below ≈ 0.02 Hz, but there was evidence for a coherence dip near 2 Hz (0.5 Hz for Observation 5). At first glance this seems consistent with both the KHT and PF models. We note, however, that the coherence function dips to as low as 0.9. Although still a large coherence

value, a dip this low is very difficult to produce by summing different *linear* transfer functions with different phase delays, *if* all the hard-to-soft variability phase differences for the individual transfer functions are approximately the same magnitude as the *observed* phase lags. On the other hand, the nonlinear transfer functions of the N94 model are seen to lead to far stronger losses of coherence, with typical coherence values being ≈ 0.1 –0.3 (Nowak et al. 1997). Such coherence values are characteristic of the coherence function observed at high frequency. (We previously have suggested that the observed loss of coherence above ≈ 3 –10 Hz may be related to nonlinear effects due to flaring activity feeding a corona on *dynamical* timescales; Nowak et al. 1998a.)

The question put forth in Vaughan & Nowak (1997) was: why are observed coherences so close to unity? With the observations presented here, and in light of the discussion of §4 and equations (3) and (4), we might wish to modify this question to: when the coherence function is so close to unity, why is it as *low* as observed? We argued in §4 that if there truly is a relationship between the time lags and the coherence, then there must be a mix of processes with a *broad* range of time lags. The fits to the phase lag and coherence data suggested one component with near zero lag between hard and soft variability. The fits further suggested that the higher frequency Lorentzian component exhibited characteristically longer time lags (at a fixed Fourier frequency) than the lower frequency Lorentzian component. This possibility was not considered in the models of N94, KHT, or PF. However, as the KHT model postulates only one ‘transfer function’ from soft variability to hard variability (i.e., diffusion through the corona), it is more difficult to reconcile this model with the conjecture that phase lags and coherence are created by a sum of independent processes. Shot noise models, however, can introduce multiple, albeit currently unknown, independent processes in the manner suggested by the fits to the data.

6. SUMMARY

We have presented timing analysis of a series of 8 RXTE observations of the black hole candidate GX 339–4. On long timescales, there is evidence of a 240 day periodicity in the ASM lightcurve. This is not a strictly periodic feature, but is probably more like a ‘characteristic timescale’. Such a timescale is consistent with warping and precession timescales (Pringle 1996; Maloney, Begelman & Pringle 1996); however, as we discuss in paper I, the evidence points more towards coronal size variations than to inclination effects.

In terms of characterizing the short timescale variability, we see that the observations break up into two sets. The seven brightest observations span a range of two in observed 3–9 keV flux and all have comparable timing properties. These observations all show evidence of an ≈ 0.3 Hz QPO. The properties of this QPO are not strictly steady; however, there are no obvious correlations with the flux of the source.

The faintest observation, which is 5 times fainter than the brightest observation, had: larger amplitude variability, characteristic PSD frequencies that were a factor of three lower than observed for the other PSDs, and showed shorter time lags between hard and soft variability. This latter feature, albeit with a great deal of scatter about the trend, was also mirrored in the flux dependence of the time lags observed for the brightest observations.

All PSDs were reasonably well-fit by the sum of three fit components: a power law, a low frequency Lorentzian, and a

high frequency Lorentzian. We further suggested that the observed Fourier frequency-dependent phase lags and coherence could be explained by summing these three components with differing intrinsic time delays between hard and soft photon variability.

We discussed all these possibilities in light of various theoretical models. The short time delays for the lowest flux observation appear to be more in agreement with ‘propagation models’ (KHT; Nowak et al. 1998b) *if the coronal size decreases with decreasing flux*. If, however, as suggested by ADAF models the coronal (i.e., advection dominated) region grows with decreasing flux, the trends observed in the time delays are *counter* to the theory. Conversely, the low flux/low frequency PSD observations are more in agreement with the models where the coronal region grows with decreasing luminosity. Shot noise models are more likely able to be adapted to explain simultaneously the phase lags and coherence as a sum of independent

linear components.

None of the models currently address the complicated nonlinear processes that may be occurring on *dynamical* timescales. Such processes, which could be the ‘flares’ that energize the corona and/or the observed radio-emitting outflow (Fender et al. 1997; Corbel et al. 1997; Hannikainen et al. 1998; paper I), could be the cause of the strong loss of coherence seen at high frequency in both GX 339–4 and Cyg X–1 (Nowak et al. 1998a), as well as the cause of the ‘flattening’ with increasing photon energy observed at the high-frequency end of the Cyg X–1 PSD (Nowak et al. 1998a).

We would like to acknowledge useful conversations with T. Aldcroft, M. Begelman, R. Fender, P. Maloney, T. DiMatteo, K. Pottschmidt, R. Staubert, and B. Vaughan. This work has been financed by NASA Grants NAG5-3225, NAG5-4731, and by a travel grant to J.W. from the DAAD.

REFERENCES

- Belloni, T., & Hasinger, G., 1990a, A&A, 227, L33
 Belloni, T., & Hasinger, G., 1990b, A&A, 230, 230
 Belloni, T., van der Klis, M., Lewin, W. H. G., van Paradijs, J., Dotani, T., Mitsuda, K., & Miyamoto, S., 1997, A&A, 322, 857
 Bendat, J., & Piersol, A., 1986, Random Data: Analysis and Measurement Procedures, (New York: Wiley)
 Corbel, S., Fender, R. P., Durouchoux, P., Sood, R. K., Tzioumis, A. K., Spencer, R. E., & Campbell-Wilson, D., 1997, in Proc. 4th Compton Symposium, ed. C. D. Dermer, M. S. Strickman, J. D. Kurfess, (Woodbury: AIP), 937
 Cowley, A. P., et al., 1991, ApJ, 381, 526
 Crary, D. J., Finger, M. H., van der Hooft, C. K. F., van Paradijs, J., van der Klis, M., & Lewin, W. H. G., 1998, ApJ, submitted
 Cui, W., Zhang, S. N., Focke, W., & Swank, J. H., 1997, ApJ, 484, 383
 Davies, S. R., 1990, MNRAS, 244, 93
 Dove, J. B., Wilms, J., Maisack, M. G., & Begelman, M. C., 1997, ApJ, 487, 759
 Esin, A. A., McClintock, J. E., & Narayan, R., 1997, ApJ, 489, 865
 Fender, R. P., Spencer, R. E., Newell, S. J., & Tzioumis, A. K., 1997, MNRAS, 286, L29
 Grebenev, S. A., Syunyaev, R., Pavlinsky, M. N., & Dekhanov, I. A., 1991, Sov. Astron. Lett., 17, 413
 Hannikainen, D. C., Hunstead, R. W., Campbell-Wilson, D., & Sood, R. K., 1998, A&A, in press
 Horne, J. H., & Baliunas, S. L., 1986, ApJ, 302, 757
 Jahoda, K., Swank, J. H., Giles, A. B., Stark, M. J., Strohmayer, T., Zhang, W., & Morgan, E. H., 1996, in EUV, X-Ray, and Gamma-Ray Instrumentation for Astronomy VII, ed. O. H. Siegmund, (Bellingham, WA: SPIE), 59
 Kazanas, D., Hua, X.-M., & Titarchuk, L., 1997, ApJ, 480, 280
 Kemp, J. C., et al., 1983, ApJ, 271, L65
 Leahy, D. A., Darbro, W., Elsner, R. F., Weisskopf, M. C., Sutherland, P. G., Kahn, S., & Grindlay, J., 1983, ApJ, 266, 160
 Levine, A. M., Bradt, H., Cui, W., Jernigan, J. G., Morgan, E. H., Remillard, R., Shirey, R. E., & Smith, D. A., 1996, ApJ, 469, L33
 Lochner, J., & Remillard, R., 1997, ASM Data Products Guide, Version Dated August 27, 1997, http://heasarc.gsfc.nasa.gov/docs/xte/asm_products_guide.html
 Lochner, J. C., Swank, J. H., & Szymkowiak, A. E., 1991, ApJ, 376, 295
 Lomb, N. R., 1976, Ap&SS, 39, 447
 Maloney, P. R., Begelman, M., & Nowak, M. A., 1998, ApJ, in press
 Maloney, P. R., & Begelman, M. C., 1997, ApJ, 491, L43
 Maloney, P. R., Begelman, M. C., & Pringle, J. E., 1996, ApJ, 472, 582
 Méndez, M., & van der Klis, M., 1997, ApJ, 479, 926
 Miyamoto, S., Kimura, K., Kitamoto, S., Dotani, T., & Ebisawa, K., 1991, ApJ, 383, 784
 Miyamoto, S., & Kitamoto, S., 1989, Nature, 342, 773
 Miyamoto, S., Kitamoto, S., Iga, S., Negoro, H., & Terada, K., 1992, ApJ, 391, L21
 Narayan, R., 1996, ApJ, 462, 136
 Nowak, M. A., 1994, ApJ, 422, 688, (N94)
 Nowak, M. A., Vaughan, B. A., Dove, J., & Wilms, J., 1997, in Accretion Phenomena and Related Outflows, ed. D. Wickramasinghe, L. Ferrario, G. V. Bicknell, (San Francisco: Astron. Soc. Pacific), 366
 Nowak, M. A., Vaughan, B. A., Wilms, J., Dove, J., & Begelman, M. C., 1998a, ApJ, in press (paper II)
 Nowak, M. A., Wilms, J., Vaughan, B. A., Dove, J., & Begelman, M. C., 1998b, ApJ, in press
 Poutanen, J., & Fabian, A. C., 1998, MNRAS, submitted (PF)
 Priedhorsky, W. C., Garmire, G. P., Rothschild, R., Boldt, E., Serlemitsos, P., & Holt, S., 1979, ApJ, 233, 350
 Priedhorsky, W. C., Terrell, J., & Holt, S. S., 1983, ApJ, 270, 233
 Pringle, J. E., 1996, MNRAS, 281, 357
 Remillard, R. A., & Levine, A. M., 1997, in All-Sky X-Ray Observations in the Next Decade, ed. N. Matsuoka, N. Kawai, (Tokyo: Riken), 29
 Scargle, J. D., 1982, ApJ, 263, 835
 Schwarzenberg-Czerny, A., 1989, MNRAS, 241, 153
 Sutherland, P. G., Weisskopf, M. C., & Kahn, S. M., 1978, ApJ, 219, 1029
 Terrell, N. J., 1972, ApJ, 174, L35
 van der Klis, M., 1989, in Timing Neutron Stars, ed. H. Ögelman, E. P. J. van den Heuvel, (Dordrecht: Kluwer), 27
 Vaughan, B. A., & Nowak, M. A., 1997, ApJ, 474, L43
 Wilms, J., Nowak, M. A., Dove, J. B., Fender, R. P., & Di Matteo, T., 1998a, ApJ, submitted (paper I)
 Wilms, J., Nowak, M. A., Dove, J. B., & Heindl, B., 1998b, ApJ, in preparation
 Zdziarski, A. A., Poutanen, J., Mikołajewska, J., Gierliński, M., Ebisawa, K., & Johnson, W. N., 1998, MNRAS, in press
 Zhang, W., & Jahoda, K., 1996, Deadtime Effects in the PCA, Technical report, (Greenbelt: NASA GSFC), version dated 1996 September 26
 Zhang, W., Jahoda, K., Swank, J. H., Morgan, E. H., & Giles, A. B., 1995, ApJ, 449, 930